3D Microstructure-based Finite Element Simulation of Cold-sprayed Al-Al₂O₃ Composite Coatings under Quasi-static Compression and Indentation Loading

Saman Sayahlatifi*, Chenwei Shao, André McDonald, James Hogan

Department of Mechanical Engineering, University of Alberta, Edmonton, T6G 1H9, Canada

*Corresponding author

E-mail: sayahlat@ualberta.ca

Phone: 1-825-436-3270

ABSTRACT

This study developed microstructure-based finite element (FE) models to investigate the behavior of cold-sprayed aluminum-alumina (Al-Al$_2$O$_3$) metal matrix composite (MMC) coatings subject to indentation and quasi-static compression loading. Based on microstructural features (i.e., particle weight fraction, particle size, and porosity) of the MMC coatings, 3D representative volume elements (RVEs) were generated by using Digimat software and then imported into ABAQUS/Explicit. State-of-the-art physics-based modelling approaches were incorporated into the model to account for particle cracking, interface debonding, and ductile failure of the matrix. This allowed for analysis and informing on the deformation and failure responses. The model was validated with experimental results for cold-sprayed Al-34 wt.% Al$_2$O$_3$ and Al-46 wt.% Al$_2$O$_3$ metal matrix composite coatings under quasi-static compression by comparing the stress versus strain histories and observed failure mechanisms (e.g., matrix ductile failure). The results showed that the computational framework is able to capture the response of this cold-sprayed material system under compression and indentation, both qualitatively and quantitatively. The outcomes of this work have implications for extending the model to materials design and for applications involving different types of loading in real-world application (e.g., erosion and fatigue).

KEYWORDS

1.   INTRODUCTION

Aluminum (Al)-based metal matrix composites (Al-MMCs) have been widely used to enhance surface performance [1-4] due to their superior mechanical properties such as high stiffness and strength [5], low coefficient of thermal expansion [6], improved wear [7] and corrosion resistance [8], and better creep-fatigue performance [9]. To fabricate Al-MMCs, a wide range of reinforcing ceramic particles (e.g., SiC [10], Al_2O_3 [1], TiC [11], TiB_2 [12] and B_4C [13]) are added to an Al matrix. Among these reinforcing particles, Al_2O_3 has been frequently used due to improved corrosion resistance and chemical stability [14]. Recently, the application of $Al-Al_2O_3$ composites fabricated by the cold-spray additive manufacturing process were used as protective coatings against wear, erosion, corrosion, and high temperature degradation in aerospace and other industrial sectors [15,16]. Among many deposition routes for producing coatings made of pure Al, cold spray stands out due to minimal heat loading of the substrate during the deposition process [17]. In addition, this additive manufacturing method provides the possibility of producing multi-phase coatings through ad-mixing feedstock powders by which the hard phases such as SiC and Al_2O_3 can be incorporated effectively in the Al-MMCs coatings [18]. These hard particles play a critical role in lowering the wear rate of the ceramic-metal coatings [19].

In research studies on experimental mechanics of ceramic-metal composite coatings, the behavior of cold-sprayed MMC coatings have been extensively addressed in terms of dry sliding wear [20], indentation [15], flexural properties [21], and erosion [16]. However, there is a limited number of articles that investigate the response of MMC coatings through computational approaches, which is addressed in the current study. For example, Bolelli *et al*. [22] generated 2D RVEs based on the SEM images of WC–CoCr and WC–FeCrAl coatings to simulate ball-on-disk test and

compression. The matrix and hard particles were modeled as elastic-plastic and pure elastic materials, respectively. The numerical results of Bolelli *et al*. [22] were compared with experiments based on the morphology of the worn surfaces and Young's modulus. In a separate study by Balokhonov *et al*. [23], 2D models at micro-, meso- and macroscales have been implemented by using the finite difference method for MMC coatings under external tension and compression. It was found that curvilinear interfaces lead to stress concentration giving rise to the formation of shear bands in the Al matrix locally as well as cracking in the ceramic particles.

From a computational perspective, the majority of previous studies on Al-MMCs have focused on axial tensile loading, by which the microstructure have been modelled via 2D [24] and 3D [25] RVEs. In a large number of studies, the occurrence of the three competitive damage mechanisms in particulate-reinforced Al matrix composites (PRAMCs) subject to tension such as matrix ductile failure, matrix/particle debonding, and particle cracking have been mainly explored by using phenomenological ductile failure criteria [25], cohesive zone models [26], and a conventional brittle cracking model [13] (i.e., elastic-cracking behavior which employs the Rankine criterion for failure initiation [48]) , respectively. For example, Zhang *et al*. [25] investigated the behavior of a 7vol.% SiCp/Al composite made by a stir casting technique and incorporated the three damage mechanisms in a real microstructure-based 3D RVE. The numerical results revealed that particle fracture and interfacial debonding emerged as the initial failure mechanisms in the composite under tensile loading.

In contrast to the numerous numerical studies that explore the tensile behavior of Al-MMCs, limited efforts have been made to address the indentation and compressive behavior

computationally, particularly with emphasis on damage mechanisms. For example, Park *et al*. [27] investigated Al-SiC MMCs under quasi-static compression up to 1% strain using a statistical synthetic RVE made by the DREAM.3D software – no damage mechanisms were incorporated into the model. The indentation behavior of MMCs has been frequently explored via 2D models [28]. More recently, Shedbale *et al*. [29] employed homogenous and heterogeneous 3D FE models to study the ball indentation response of particulate-reinforced MMCs. The results showed that the heterogeneous model tends to overestimate the hardness compared to the experiments due to the local concentration of particles under the indenter.

Motivated by previous numerical studies, which primarily focus on the tensile response of MMCs, this work aims to investigate the compressive and indentation behavior of Al-Al_2O_3 coatings by using 3D RVEs produced by Digimat software based on microstructural characteristics obtained using scanning electron microscope images. To account for the damage mechanisms, the Gurson–Tvergaard–Needleman (GTN) model [30] was applied to the Al matrix and the matrix/particle debonding was modelled by the CZM method [31]. For the ceramic particle phase, the Johnson-Holmquist II (JH2) model [32] was used to incorporate particle cracking into the FE model. The model was validated with the experimental data for Al-34 wt.% Al_2O_3 and Al-46 wt.% Al_2O_3 coatings in terms of stress-strain histories, failure mechanisms, and Vickers hardness. The results show that the model has the potential to be employed for parametric studies for material design and optimization, which tailors concentration of reinforcing particles to balance strength and density for weight-sensitive applications.

2.   EXPERIMENTAL PROCEDURES

2.1. *Material and specimen preparation*

In this study, pure Al and Al-Al$_2$O$_3$ composite coatings were fabricated using a low-pressure cold spray system (SST series P, CenterLine, Ltd., Windsor, ON, Canada), as shown schematically in Fig. 1(a), which was connected to a volumetric powder feeder (5MPE, Oerlikon Metco, Westbury, NY, USA). Based on previous studies [2,33,34], the air temperature and pressure were set to 375 °C and 620 kPa, respectively. The nozzle was manipulated by a robot (Motoman HP-20, Yaskawa Electric Corp., Waukegan, IL, USA). The cold-spray nozzle traversed across the Al substrate at a speed of 15 mm/s to transfer the feedstock powder to the substrate, and the deposition process produced 5 layers of the coating. The feedstock powder blend was developed through a three-step process: gas atomization, sieving, and mixing (see Fig. 1(a)). Aluminum (99.0%) powder (CenterLine, Ltd., Windsor, ON, Canada) and α-Al$_2$O$_3$ with a purity of 99.5% (Amdry 6060, Oerlikon Metco Inc., Westbury, NY, USA) was used in this study. The Al and Al$_2$O$_3$ powders were sieved to obtain a size distribution of 40-60 μm and 30-45 μm, respectively. The Al and Al$_2$O$_3$ powders were admixed to produce powder blends containing 0, 60, and 90 wt.% Al$_2$O$_3$. This process was conducted using a cylinder with a 20 mm diameter whose angular velocity and operating time was set to 20 RPM and 30 minutes, respectively. As shown by Shao *et al.* [33], when deposited into coatings, the mixed powder blend with 60 wt.% Al$_2$O$_3$ produced coatings that were Al-34 wt.% Al$_2$O$_3$ and the mixed powder blend with 90 wt.% Al$_2$O$_3$ produced coatings that were Al-46 wt.% Al$_2$O$_3$.

2.2. *Mechanical testing and characterization*

As shown in Fig. 1(b), the cold-sprayed coating deposits were cut into cuboidal specimens with dimensions of 2.3 mm in length, 2.7 mm in width, and 3.5 mm in height using wire electrical

discharge machining. The samples were used for quasi-static compression testing, where the loading was applied in the direction of the 3.5 mm dimension. The experiments were conducted using the displacement control technique up to a maximum displacement of 1 mm at a constant rate of 1×10^{-3} s^{-1} using an Instron 3365 testing machine (Instron, Norwood, Massachusetts, USA). To visualize the features of the macroscopic deformation of the specimen surface, the machine was equipped with an AOS PROMON U750 high-speed camera with a full resolution of 1280 × 1024 and a VIC 900170WOF LED laser light guide for illumination. This assembly was coupled with digital image correlation (DIC) capabilities using VIC-2D (v6 2018) software [35] (Correlated Solutions Irmo, SC, USA) to monitor the strain fields, which is detailed in Shao *et al*. [33]. The specimen was aligned between the loading platens made from M2-graded high-speed steel with a diameter of 1 inch (see Fig. 1(b)), and extreme pressure grease was applied on the interfaces to eliminate the effect of friction and allow free lateral expansion. The compression tests were carried out as per ASTM Standard C1424-15 [36] at room temperature and repeated 4 times for each coating with different reinforcing particle content. To inform the microstructure-based models as related to the reinforcing particle content, porosity, particle shape, size, and distribution, microstructural characterization was done using a field-emission SEM coupled with energy-dispersive X-ray spectroscopy (EDS) operated at 20 kV (Zeiss Sigma, Oberkochen, Baden-Württemberg, Germany), as shown in Fig. 1(c) for the Al-46 wt.% Al$_2$O$_3$ composite. The porosity of the samples was estimated using ImagePro software coupled with the SEM images, and it was found to be 2.84 ± 0.31 vol% in pure Al, 0.23 ± 0.04 vol% in Al-34 wt.% Al$_2$O$_3$, and 0.17 ± 0.03 vol% in Al-46 wt.% Al$_2$O$_3$. In addition, the EDS analysis revealed that the feedstock powders with 60 and 90 wt.% Al$_2$O$_3$ led to depositions with 34 ± 2.56 wt.% and 46 ± 2.04 wt.% of ceramic particles, respectively.
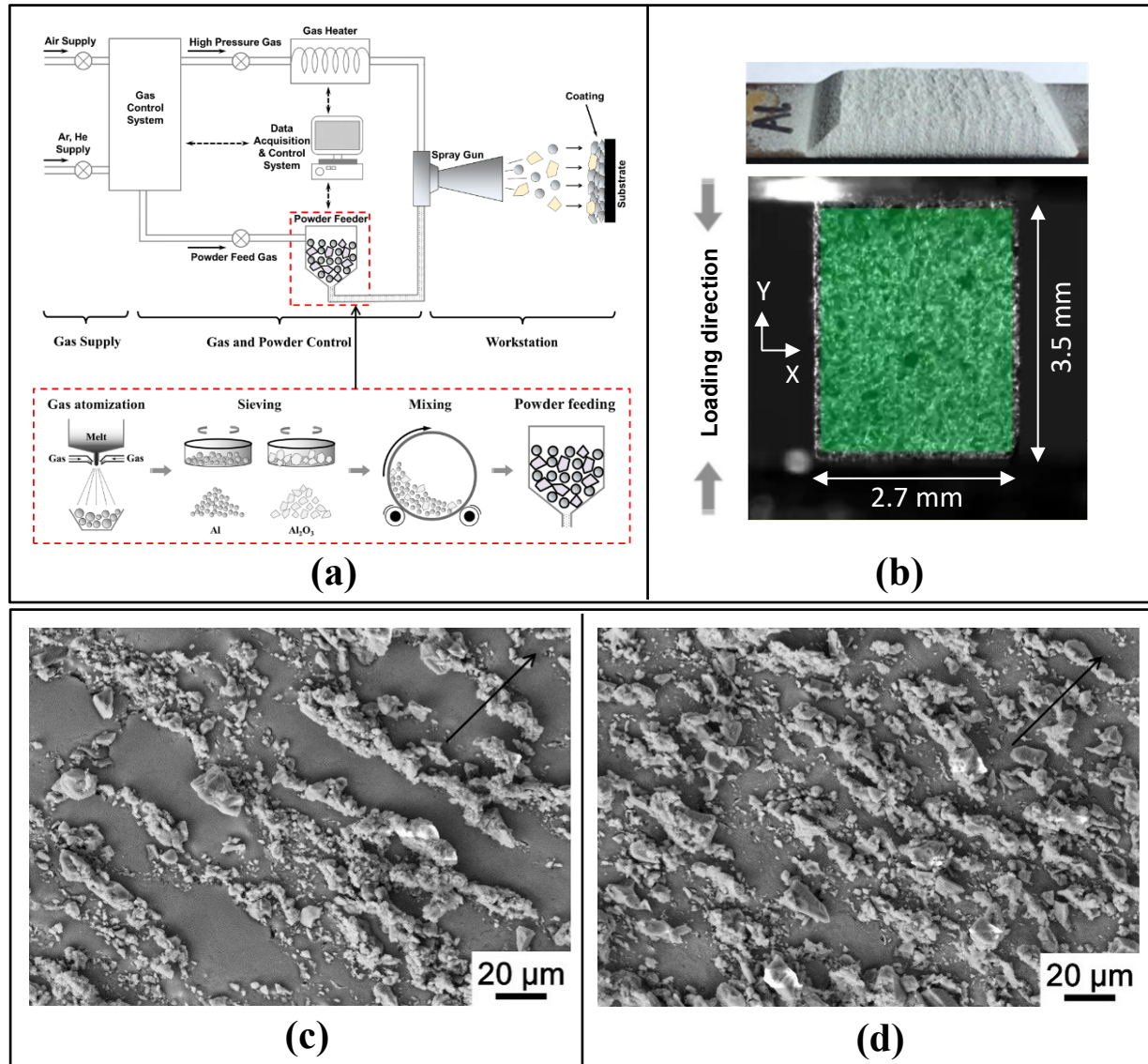
Fig. 1. Preparation, test, and characterization of Al-Al$_2$O$_3$ composite coatings: (a) A schematic illustration of the cold spray setup used for the fabrication of pure Al and MMC coating samples: The processing strategy for making the mixed powder includes gas atomization, sieving, and mixing using a rotated cylinder; (b) Typical compressive cuboidal specimen with dimensions 2.3 mm × 2.7 mm × 3.5 mm cut from the composite depositions via wire electrical discharge machining, which was loaded in the direction of the 3.5 mm dimension. The green contour shows the region of interest defined on the specimen surface in VIC-2D software for monitoring the strain fields. The top image shows an example of Al-Al$_2$O$_3$ coating deposited on an Al substrate from which the cuboidal specimens were cut; (c) SEM characterization of the microstructure of Al-34 wt.% Al$_2$O$_3$ composite coating showing the distribution and morphology of the reinforcing ceramic particles in the Al matrix; (d) SEM micrograph of Al-46 wt.% Al$_2$O$_3$ composite coating. Note that the black arrows on the SEM micrographs show the deposition direction. The darker regions correspond to the Al phase and the lighter regions correspond to the alumina phase.

3. NUMERICAL METHODOLOGY

A 3D FE model based on coating microstructural features is presented to explore the behavior of Al-Al$_2$O$_3$ MMC coatings under quasi-static compressive loading. The 3D representative volume elements (RVEs) were generated by the Digimat Software for Al-34 wt.% Al$_2$O$_3$ and Al-46 wt.% Al$_2$O$_3$ MMCs. The RVEs were imported into the ABAQUS/Explicit solver (release 6.14). For the micro-indentation test, the homogenization approach [29] was applied and experimental compression data was used to extract the effective mechanical properties for each MMC coating sample.

3.1. *Geometry and model description*

RVEs with different sizes have been considered in previous studies [13,37]. For example, Ma *et al*. [37] found no significant difference in the tensile stress-strain responses by varying the RVE size from 20 μm to 50 μm. In this study, an RVE length of 100 μm was chosen based on the microstructural features (e.g., average reinforcing particle size of 15 μm). The SEM images (see Fig. 1(c) and (d)) were first used to extract the distribution of particle size in the composites (e.g., the size of the alumina particles range from 1 to 30 μm in the Al-46 wt. % Al$_2$O$_3$ composites (see Fig. 1(c)). Next, the measured range of distribution was incorporated into the RVE using a uniform distribution in the Digimat software, which allows to account for the variation and uncertainty in the particle size distribution that is likely to be observed through the SEM images from different locations of the sample. Additionally, the reinforcing ceramic particles represent an irregular shape in the SEM micrographs. Here, icosahedron geometry was used to account for the shape of the particles, which has also been used to represent the irregular-shaped particles in previous studies [37-39]. The time step was set at 2 μs, which was found to meet the quasi-static loading condition

[40]. As shown in Fig. 2(a), the top and bottom boundary faces have been fully restricted to the reference points (RPs) by the kinematic coupling constraints to facilitate application of load/boundary conditions and obtain the stress-strain response of the RVE. A corner of the RVE was fully restricted to prevent the material from rigid boundary motion. The degrees of freedom of the bottom boundary face were fixed within all degrees of freedom, except for the in-plane displacements (i.e., Y- and Z-directions in Fig. 2(b)). The same boundary conditions for application of compressive loading were also used in other studies [41,42]. All of the constituents were discretized by 3D linear tetrahedral C3D4 elements. Following a mesh quality assessment to decrease the likelihood of element distortion at high strains, an average element size of 1.5 μm was used. On this basis, the RVE for Al-34wt.% Al_2O_3 and Al-46wt.% Al_2O_3 MMCs were meshed by 741,222 and 1,275,358 elements, respectively. Micro-indentation Vickers testing of the composite coatings was simulated via the homogenization approach [29]. The effective mechanical properties, including the Young's modulus and flow stress, were extracted from the experimental compressive stress-strain histories for each particle concentration in the coatings and was an input into the approach. Figure 3 shows the FE model of the Vickers test. Due to symmetry, only one quarter of the homogenized block with symmetric constraints was modelled. The size of the block was determined as per the work of Shedbale *et al*. [29] to achieve convergence in the indentation response.
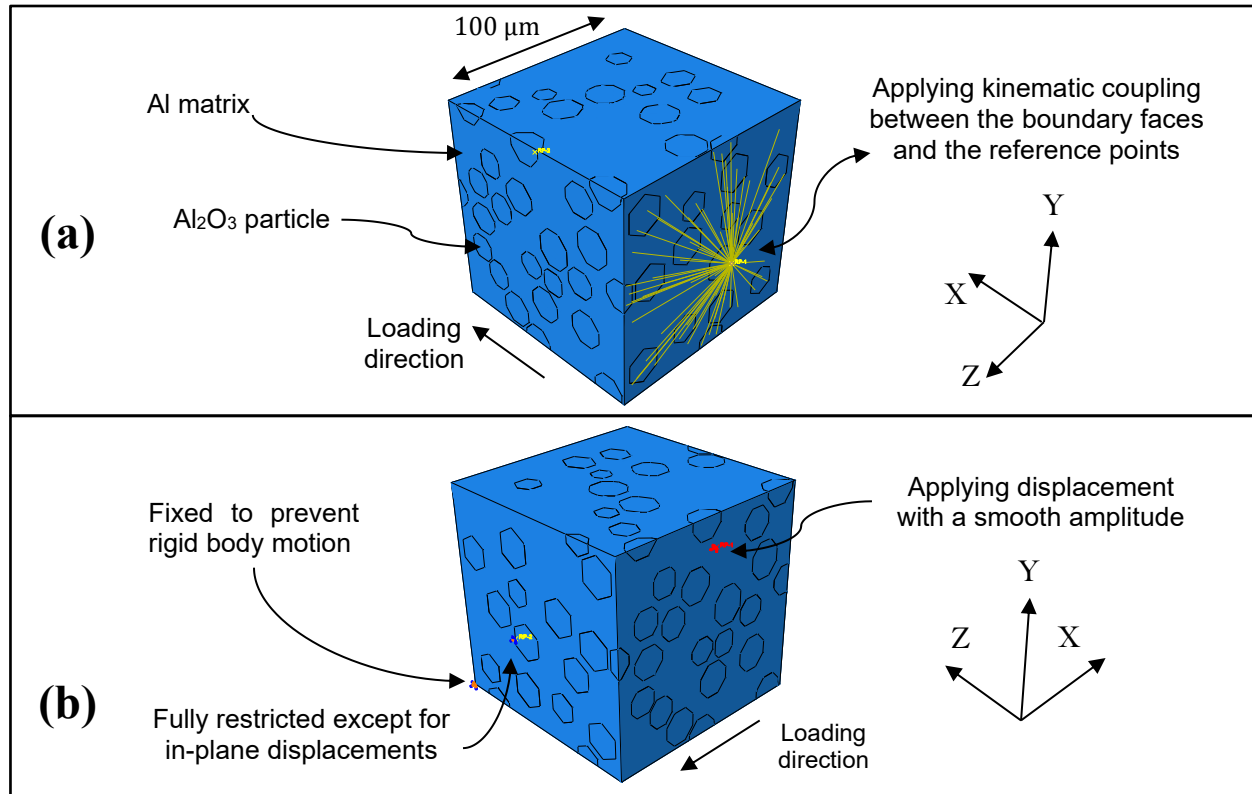
Fig. 2. (a) Application of kinematic coupling between the boundary faces and the reference points (RP) in yellow color to apply compressive load and boundary conditions: All degrees of freedom were coupled to each other; (b) The boundary conditions applied on the RVE: The displacement control technique was applied to the RP in red color using a smooth amplitude to meet the quasi-static condition.
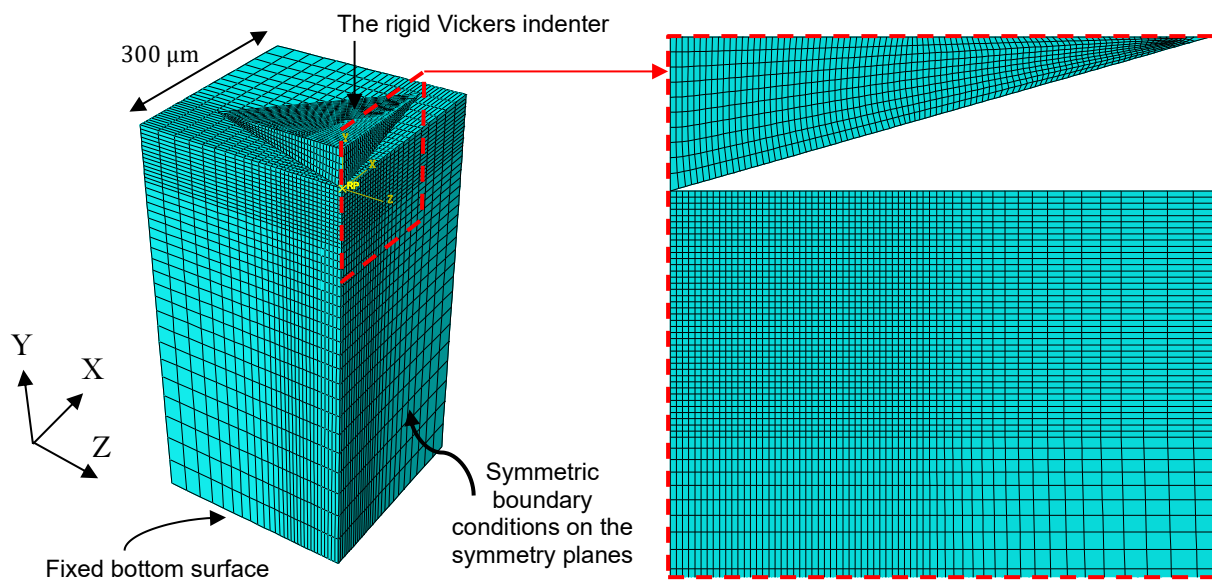

Fig. 3. Finite element model of the micro-indentation Vickers test. The block and the indenter were discretized by 30,276 first order 8-node 3D elements with reduced integration (C3D8R) and 2104 quadrilateral 4-node 3D rigid elements (R3D4), respectively.

9

As shown by Shedbale *et al*. [29], the Vickers indenter was considered as a discrete rigid body and fully confined, except for the vertical direction Y (see Fig. 3). The bottom surface of the block was fixed, and the lateral surfaces were free to deform. A frictionless contact was defined between the indenter and the top surface of the block, which was implemented by the standard surface-to-surface contact algorithm [29]. By using an average element size of 5 μm, the block and the indenter were meshed by using 30,276 first order 8-node 3D elements with reduced integration (C3D8R) and 2104 quadrilateral 4-node 3D rigid elements (R3D4), respectively.

3.2. *Material models*

In this study, the micromechanical-based Gurson–Tvergaard–Needleman (GTN) model [30] was applied to capture the matrix failure. Given experimental evidence of particle cracking and interfacial debonding under compression, the Johnson-Holmquist II (JH2) model [32] for the failure of ceramic particles and the cohesive zone model (CZM) approach [31] for the matrix/particle debonding failure were incorporated into the model.

3.2.1. *The GTN model for matrix failure*

Ductile failure of metals occurs as a result of a three-stage mechanism of nucleation, growth, and coalescence of voids. Voids are nucleated from an inclusion or as a consequence of either cracking or decohesion of second phase particles and then grow due to the localization of plastic strain under a high stress triaxiality state [43]. To analyze this phenomenon theoretically, the porous metal plasticity model proposed by Tvergaard and Needleman (i.e., the GTN model) [30], as a modified version of the Gurson model [44], has been widely used [45-47]. The yield function of the GTN model is expressed as follows:

$$\emptyset(\sigma, f) = \left(\frac{\sigma_q}{\sigma_y}\right)^2 + 2q_1 f^* cosh\left(\frac{3q_2 p}{2\sigma_y}\right) - \left(1 + q_3 f^{*2}\right) = 0, \tag{1}$$

where $\emptyset$ denotes the non-dilatational strain energy and q_1, q_2, and q_3 are the constants proposed by Tvergaard [48] to account for the effects induced by void interaction due to multiple-void arrays and to provide better consistency with experimental data. Here, σ_q and σ_y represent von Mises stress and the flow stress of the undamaged material. To model the rapid deterioration of stress carrying capacity caused by void coalescence, the parameter, f^*, known as the effective porosity was first introduced by Tvergaard-Needleman [30]. The function is specified as follows:

$$f^* = \begin{cases} f & f \le f_c \\ f_c + \frac{f_u^* - f_c}{f_F - f_c}(f - f_c) & f_c \le f \le f_F \\ f_u^* & f \ge f_F \end{cases}, \tag{2}$$

where f_c is the critical void volume fraction (VVF) at the onset the of coalescence, $f_u^* = \frac{1}{q_1}$ corresponds to zero stress carrying capacity, and f_F denotes the VVF when the material has completely failed, which governs the element deletion process. The increase in the VVF is deemed as the summation of the increment owing to void nucleation and the growth of the existing voids. The function can be written as:

$$df = df_{nucleation} + df_{growth} \,. \tag{3}$$

Assuming plastically incompressible behavior for the material, the void growth rate (i.e., df_{growth}) can be expressed as a function of the plastic volume change as follows:

$$df_{growth} = (1 - f)d\varepsilon_{ii}^p, \tag{4}$$

where $d\varepsilon_{ii}^p$ denotes the trace of the plastic strain rate tensor. The nucleation of voids is considered to be exclusively dependent on the plastic strain and it was assumed that occurrence of void

nucleation occurred only under hydrostatic tension [49,50]. On this basis, the function is written

as:

$$df_{nucleation} = A_n d\bar{\varepsilon}_m^p \text{ , where} \tag{5}$$

$$A_n = \begin{cases} \dfrac{f_N}{s_N\sqrt{2\pi}} e^{-0.5\left(\frac{\bar{\varepsilon}^p - \varepsilon_N}{s_N}\right)^2} & if\ p \geq 0 \\ 0 & if\ p < 0 \end{cases}, \tag{6}$$

where p represents the hydrostatic stress, f_N is the void volume fraction of the nucleated void, ε_N

is the mean equivalent plastic strain for void nucleation, and s_N is the standard deviation of the

distribution. Here, the rate of equivalent plastic strain, $d\bar{\varepsilon}^p$, is obtained by enforcing equality

between the matrix plastic dissipation and the rate of macroscopic plastic work as follows:

$$d\bar{\varepsilon}^p = \frac{\sigma : d\varepsilon^p}{(1-f)\sigma_y}. \tag{7}$$

Table 1 summarizes the constants of the GTN model used in this study. The proposed values by

Tvergaard [48] were utilized for the q_1, q_2, and q_3 constants. From SEM characterization, the

initial porosity, f_0, was assumed to be an average quantity of 0.0017 and 0.0023 for Al-34 wt.%

Al_2O_3 and Al-46 wt.% Al_2O_3 composites, respectively. The parameters ε_N, s_N, and f_N were

obtained from previous studies for pure Al [39,51].

Table 1. GTN model constants used in this study. Here, the value of f_0 corresponds to the composites with 34wt.% of reinforcing particles. For Al-46 wt.% Al_2O_3 composites, the initial porosity was determined to be 0.0023 on average, while all other constants remain the same as the 34 wt.% case.

q_1 [48]	q_2 [48]	q_3 [48]	f_0 [33]	f_c [51]	f_F [51]	ε_N [39]	s_N [39]	f_N [51]
1.5	1	2.25	0.0017	0.1	0.45	0.3	0.1	0.25

3.2.2. *The JH2 model for particle cracking*

For damage modeling of ceramics, the phenomenological Johnson-Holmquist models have been commonly used [38,52-54] to depict the behavior of these materials, including pressure-dependent strength, strain-rate dependency, and dilation or bulking effects [32]. The strength and damage are expressed as analytical functions of pressure and other parameters as [32]:

$$\sigma^* = \sigma_i^* - D(\sigma_i^* - \sigma_f^*), \tag{8}$$

$$\sigma_i^* = A(P^* + T^*)^N(1 + Cln\dot{\varepsilon}^*), \text{ and} \tag{9}$$

$$\sigma_f^* = B(P^*)^M(1 + Cln\dot{\varepsilon}^*) \leq SFMAX, \tag{10}$$

where σ^* and σ_i^* represent the normalized intact equivalent stress, σ_f^* denotes the normalized fracture stress, and D is the damage variable, varying from 0 to 1. Here, $\sigma^* = \sigma/\sigma_{HEL}$, $P^* = P/P_{HEL}$, $T^* = T/P_{HEL}$, and $\dot{\varepsilon}^* = \dot{\varepsilon}/\dot{\varepsilon}_0$, where σ is the actual equivalent stress, σ_{HEL} is the equivalent stress at the Hugoniot elastic limit (HEL), P is the actual pressure, P_{HEL} is the pressure at the HEL, T is the maximum tensile hydrostatic pressure tolerated by the material, $\dot{\varepsilon}$ is the actual strain rate, and $\dot{\varepsilon}_0 = 1$ is the reference strain rate. $A, B, C, M,$ and N are material constants which need to be calibrated for each material. The maximum value of σ_f^* is defined by $SFMAX$ (i.e., the maximum limitation of the normalized fractured strength). Once the yield function is met as per Eq. (11), the damage begins to accumulate based on the incremental equivalent plastic strain defined as:

$$\emptyset(\sigma, f) = \sigma_q - \sigma_{HEL}\sigma^* \geq 0, \tag{11}$$

$$D = \sum \frac{\Delta\varepsilon_{eff}^p}{\varepsilon_f^p}, \text{ and} \tag{12}$$

$$\varepsilon_f^p = D_1(P^* + T^*)^{D_2}, \tag{13}$$

13

where σ_q, D_1, and D_2 are deemed as material constants. To calculate pressure, P, a polynomial equation of state (EOS) is employed, which is defined as:

$$P = \begin{cases} K_1\eta + K_2\eta^2 + K_3\eta^3 + \Delta P & \eta > 0 \\ K_1\eta & \eta \le 0 \end{cases}, \tag{14}$$

$$\Delta P_{t+\Delta t} = -K_1\eta_{t+\Delta t} + \sqrt{(K_1\eta_{t+\Delta t} + \Delta P_t)^2 + 2\beta K_1 \Delta U}, \tag{15}$$

$$\Delta U = U_t - U_{t+\Delta t}, \text{ and} \tag{16}$$

$$U = \frac{\sigma_y^2}{6G}, \tag{17}$$

where K_1 denotes the bulk modulus, K_2 and K_3 are material constants, η is the specific volume, U represents the internal energy which is related to the equivalent plastic flow stress σ_y by a quadratic expression, β is the fraction of the elastic energy loss converted to potential hydrostatic energy, and the shear modulus is shown by G. The 21 constants of the JH2 model for Al$_2$O$_3$ were obtained from previous studies [54,55], and are summarized in Table 2.

Table 2. The JH2 constants used for Al$_2$O$_3$ reinforcing particles [54,55].

Parameter	Value	Unit
A	0.93	-
B	0.31	-
N	0.6	-
M	0.6	-
C	0	-
K_1	193	GPa
K_2	0	GPa
K_3	0	GPa
d_1	0.005	-
d_2	1	-
ρ	3890	kg/m^3
G	155	GPa
T	0.6	GPa
HEL	10.5	GPa
P_{HEL}	4.5	GPa
$\sigma_{i,max}$	12.2	GPa
$\sigma_{f,max}$	1.3	GPa
$\varepsilon_{f,min}$	0	-
$\varepsilon_{f,max}$	1.2	-
FS	0.2	-
β	1	-

3.2.3. *The cohesive zone model for the interfacial debonding*

The cohesive zone model (CZM) was first proposed by Barrenblatt [31] and Dugdale [56] and is now widely used as an effective approach for modeling the fracture process in materials such as polymers, metals, ceramics, concretes and laminated composites [57]. It was assumed that matrix/particle interface debonding occurs when the quadratic interaction function involving the nominal stress ratios attains unity as follows [58]:

$$\left(\frac{T_n}{T_n^0}\right)^2 + \left(\frac{T_s}{T_s^0}\right)^2 + \left(\frac{T_t}{T_t^0}\right)^2 = 1, \tag{18}$$

where, T_n, T_s, and T_t represent the tractions acting on the interface at a load increment in normal and in two in-plane shear directions, respectively. Likewise, T_n^0, T_s^0, and T_t^0 denotes the tractions at the onset of damage initiation in normal and in two in-plane shear directions. Note that the normal traction is tensile and pure compressive stress does not lead to decohesion. The components of the traction-separation law are written as follows:

$$T_n = \begin{cases} (1-D)T_n^* & T_n^* \geq 0 \\ T_n^* & T_n^* < 0 \end{cases}, \tag{19}$$

$$T_s = (1-D)T_s^*, \text{ and} \tag{20}$$

$$T_t = (1-D)T_t^*, \tag{21}$$

where T_n^*, T_s^*, and T_t^* are the stress components calculated by the elastic traction-separation behavior for the current strain prior to the damage initiation. D denotes the damage variable which begins to gradually increase from 0 to 1 with further loading once the debonding initiation criterion expressed by Eq. (18) is met. The damage variable is defined as [58]:

$$D = \begin{cases} 0 & \delta_m^{max} \leq \delta_m^0 \\ \dfrac{\delta_m^f(\delta_m^{max} - \delta_m^0)}{\delta_m^{max}(\delta_m^f - \delta_m^0)} & \delta_m^0 < \delta_m^{max} < \delta_m^f, \\ 1 & \delta_m^{max} > \delta_m^f \end{cases} \tag{22}$$

where, δ_m^0 and δ_m^f represents the effective separations at damage initiation and complete failure, respectively. The maximum value of the effective displacement during the loading process at each increment is shown by δ_m^{max}. The effective separation at each load increment δ_m is calculated as [58]:

$$\delta_m = \sqrt{\delta_n^2 + \delta_s^2 + \delta_t^2}, \tag{23}$$

where, δ_n, δ_s, δ_t are the nominal separations in normal and in two in-plane shear directions, respectively. To obtain the effective separation at complete decohesion, one can use the fracture energy G_c, which is given as:

$$\delta_m^f = \frac{2G_c}{T_n^0}. \tag{24}$$

The CZM constants used in this study are presented in Table 3. For Al-MMC composites, the CZM constants have been reported in different ranges in the previous studies [13,59-62]. For example, the reported values for the interface strength varies from a quantity on the order of MPa [61] to GPa [62]. The values in Table 3 were selected to establish the best match between the experimental and numerical outcomes in this research study.

Table 3. Summary of the matrix/particle interface properties.

Parameter	K_{nn}, K_{ss}, K_{tt}	T_n^0, T_s^0, T_t^0 [61]	δ_m^f [61]
Value	2E7 MPa.mm^{-1}	705 MPa	0.00035 mm

4. RESULTS

4.1. *Quasi-static compression*

The numerically predicted results for Al-34 wt.% Al_2O_3, and Al-46 wt.% Al_2O_3 coatings under quasi-static compression are compared with those of the experiments in terms of the stress versus strain histories and observed failure mechanisms. This can provide insights for establishing an accurate computational framework to further explore the behavior of the material that can eventually give rise to a tool for material design and optimization. Shown in Fig. 4 is the predicted stress-strain responses in comparison to those measured by experiments. The pure Al and MMC samples were all experimentally tested in different directions, namely the nozzle traverse (travel) direction, the second in-plane direction perpendicular to the nozzle travel direction, and the deposition direction represented by X, Y, and Z, respectively, in Fig. 4.

For the pure Al matrix, the results based on the data for the Z-direction was compared to the experiment, as shown in the red solid curve in Fig. 4. The predicted curve for the pure Al matrix aligns with the experimentally measured one, which shows the accuracy of the approach for modeling the pure Al coating. Regarding the predicted responses for the MMCs, the model can reasonably capture the stiffness (i.e., the Young's modulus) and the maximum load bearing capacity of the composite coatings with different reinforcing particle concentrations. In addition, the experimental trend towards decreasing ductility with increase in reinforcing particle content from 34 wt.% to 46 wt.% is reasonably reflected in the numerically predicted curves. Namely, plastic deformation in the Al-34 wt.% Al_2O_3 composite coating begins to take place in the model at a strain of 0.6%, which leads to a yield stress of 141 MPa. The experimental yield strain ranges
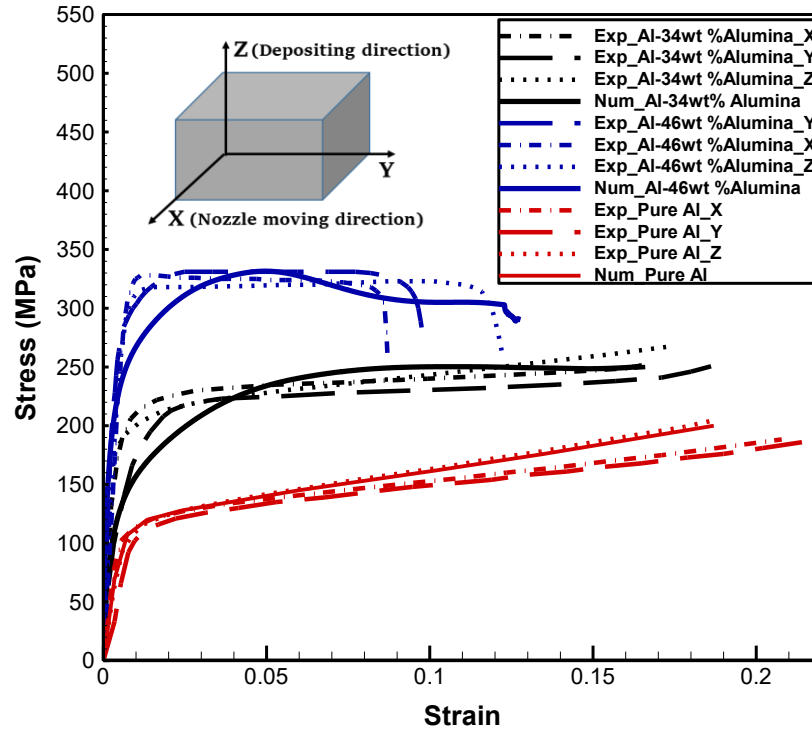
Fig. 4. Numerical (Num) and experimental (Exp) stress-strain responses under quasi-static compression for different weight percentage of alumina in the Al matrix. The cuboidal samples were all tested in three different directions denoted by X, Y, and Z corresponding to the nozzle moving direction, the second in-plane direction perpendicular to the nozzle moving direction, and the deposition direction, respectively. The dashed curves correspond to the experimental responses for each coating and the solid curves represent the associated numerically predicted behavior.

from 0.53% to 0.65% and yield stress ranges from 135 MPa to 178 MPa based on the different

coordinate directions that were explored. The model tends to slightly underestimate the yield stress

of the MMC with 34wt% of the reinforcing inclusions. This is likely due to cold working, which

introduces a hardening and strengthening effect in the matrix during the cold spray process. This

is a result of the high-velocity hard ceramic particles impacting on the Al grains [18,63], which is

not yet considered in the model. In addition to cold working phenomenon, there are also other

mechanisms that are likely to cause the deviations between the predicted and experimental stress

versus strain histories in terms of the strain hardening behavior, and elongation at failure. Among

these mechanisms, one can cite the grain size effects [64,65] (e.g., Hall-Petch relationship [66])

which require the implementation of strain gradient plasticity models [67] to be incorporated in

Figure 5 illustrates the contour of the plastic deformation [68], interfacial failure [26], and particle cracking [24] at two different axial strains during the loading process for the Al-34 wt.% Al_2O_3 composite. With further application of load, the plastic strain begins to accumulate in the ligament between the particles closely aligned together (see Fig. 5(a)), which has been reported in previous studies of 2D RVEs [68]. The localization of plastic strain leads to the growth of void volume fraction in the matrix resulting in a gradual decrease in matrix flow stress (see the solid black curve in Fig. 4). In addition, as the strain exceeds 4%, matrix/particle debonding and a particle cracking failure mechanism manifest and develop with the increase in applied load within the RVE (see Fig. 5(b) and (c)), particularly at the sharp corner and concaves of the particles [68]. This behavior can be attributed to the mismatch between the mechanical constants as well as the stress concentration at the curvilinear interfaces [23]. Consequently, the flow stress remains almost constant from 5% strain to a strain of 15%, and then rises slightly with further increase in load up to the end of the loading cycle. This behavior is also reflected in the experimental curves, as matrix failure happens locally and does not lead to fracture of the sample (Fig. 4 - the dashed curves for the 34 wt.% Al_2O_3 MMCs). From simulation, it can be implied that spatial distribution of the particles affected by the number of particles and the mean free path parameter (i.e., inter-particle spacing of the reinforcing phase) [69] – which is determined by the weight percentage of the inclusions – does not lead to fracture of the Al-34 wt.% Al_2O_3 MMC sample, since the number of thin ligaments is not critical enough to develop a 45° shear band [13,68], fracturing the specimen. This numerical implication (i.e., the micro cracks in the matrix do not evolve to fracture the

For the Al-46 wt.% Al_2O_3 composite, the predicted yield strain and yield strength are 0.7% and 253 MPa, respectively, while the measured yield strain varies between 0.79% and 0.83% and yield strength varies between 298 MPa and 317 MPa for the different coordinate directions. The larger discrepancy in the predicted yield stress of the Al-46 wt.% Al_2O_3 MMC compared to that of the Al-34 wt.% Al_2O_3 MMC can be another indication of the importance of including the cold spray-induced hardening and strengthening effect in the model in order to produce more accurate numerical results, especially for the MMCs with a high percentage of particle reinforcement. Additionally, the earlier onset of the debonding failure mechanism in the model compared to the experiments can also play a role in the loss of stiffness prior to achieving peak load.

Figures 6 and 7 draw a comparison between the predicted and experimentally observed failure mechanisms in the Al-46 wt.% Al_2O_3 composite. As shown, the FE model can capture the occurrence of the three competitive damage mechanisms (i.e., matrix ductile failure, matrix/particle debonding, and particle cracking) of metal-ceramic coatings under compressive loading. In comparison to the MMC coating with 34 wt.% alumina reinforcement, the plastic strain is severely localized in the thin ligaments between the particles (see Fig. 6(a)) in the model. The model predicts the formation of $45^°$ shear cracks passing through the Al matrix between the particles as observed in SEM images, as shown in Fig. 7. Once the strain exceeds 4%, particle cracking and matrix/particle debonding are initiated at the sharp corners of the particles (see Fig-
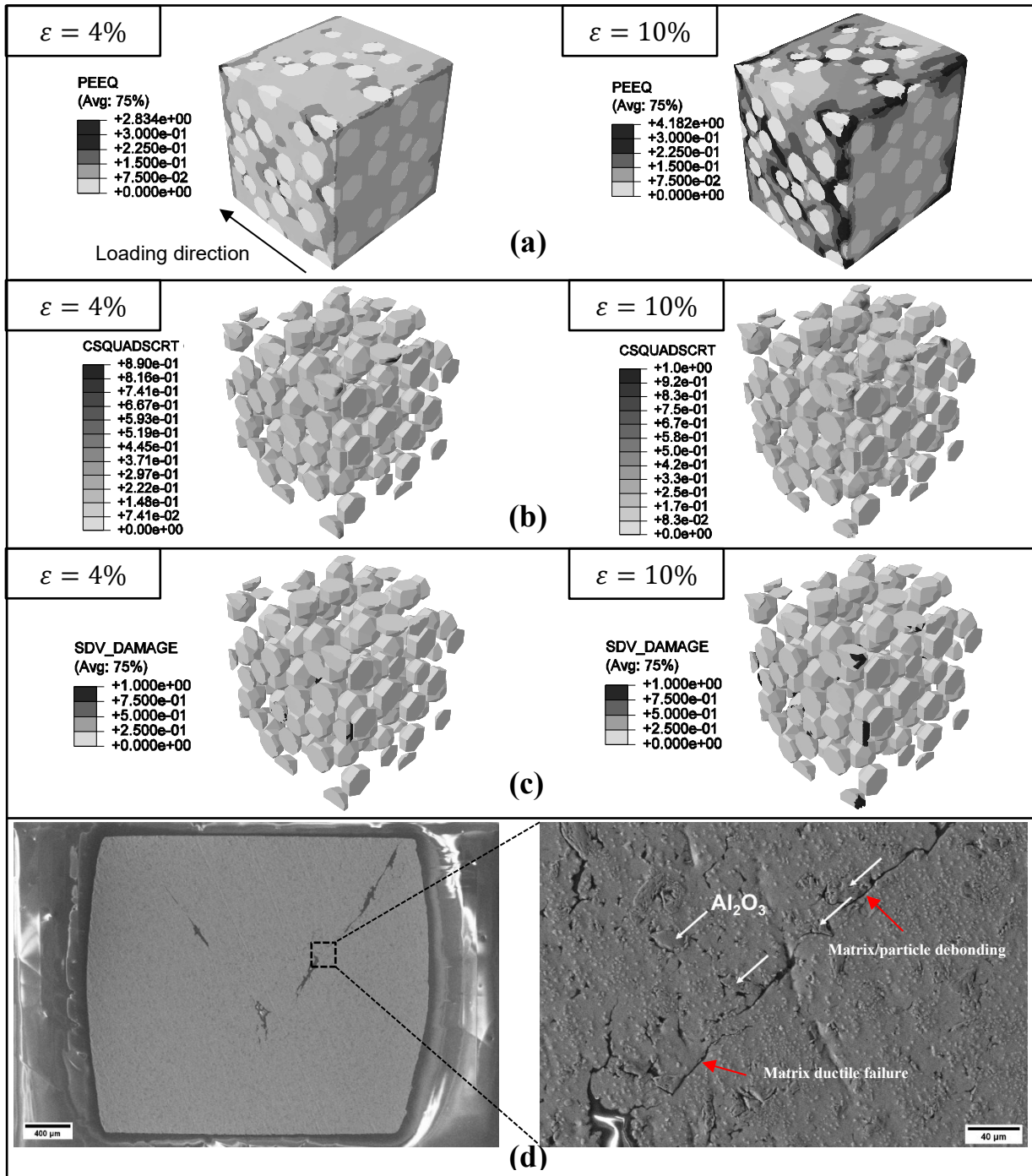
Fig. 5. The numerically predicted manifestation and evolution of the damage mechanisms in Al-34 wt.% Al$_2$O$_3$ MMC at an axial strain of 4% and 10%: (a) The equivalent plastic strain (PEEQ), which reveals the evolution of plastic deformation in the thin ligaments between the ceramic particles; (b) The data shows the scatter of matrix/particle debonding failure criterion demonstrating the initiation of interfacial failure at the sharp corners of inclusions; (c) The distribution of the JH2 damage parameter shows the accumulation of damage and element removal in the concaves of particles either at the boundary surfaces or considerably close to each other; (d) SEM micrograph of the Al-34 wt.% Al$_2$O$_3$ MMC subject to quasi-static compression showing the localized occurrence of damage mechanisms (e.g., matrix ductile failure, and matrix/particle decohesion) at micro length scale that does not lead to the coalescence of micro cracks and global failure of the composite at macro scale.
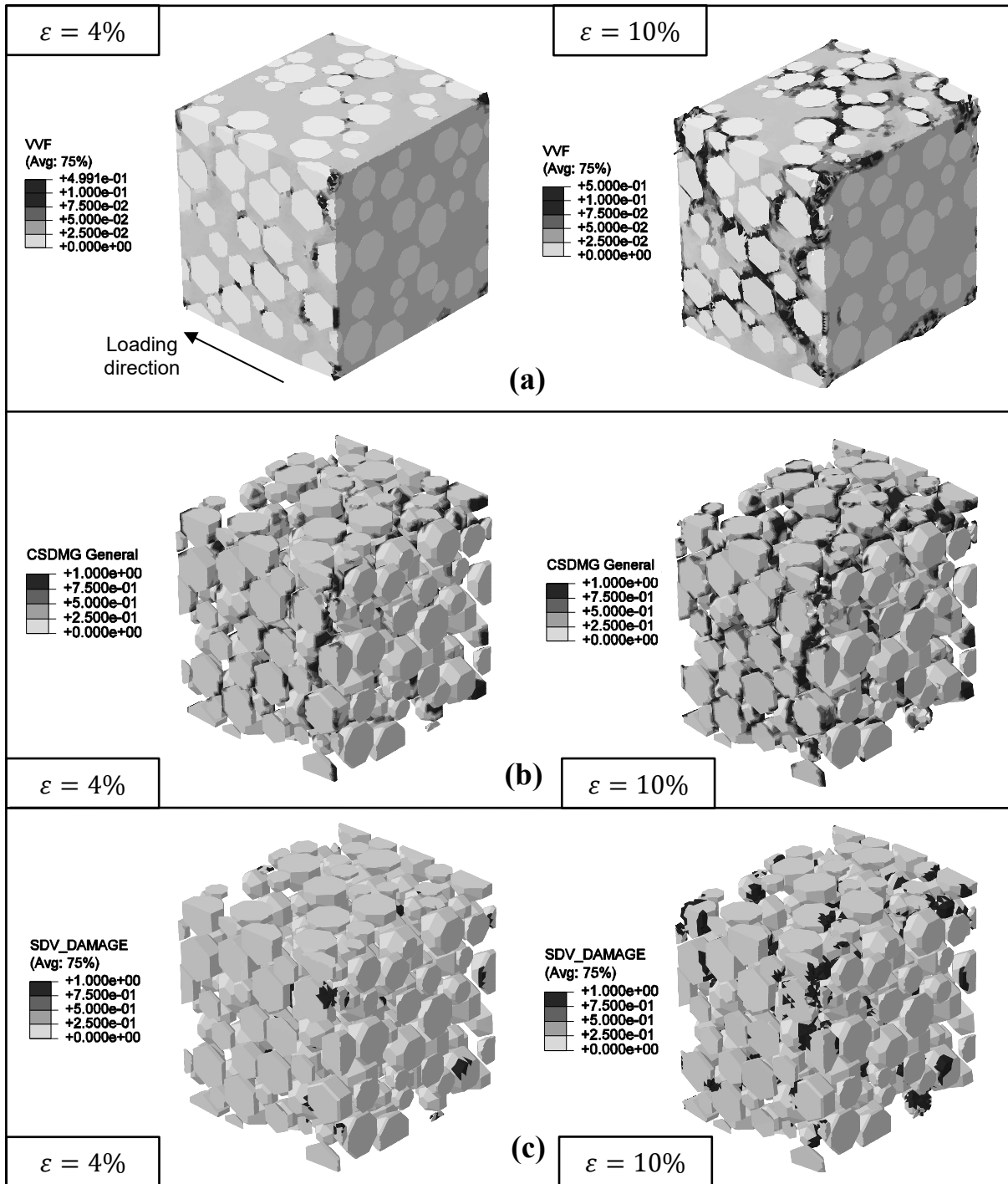
21

Fig. 6. The numerical qualitative results for the Al-46 wt.% Al$_2$O$_3$ MMC shown at an axial strain of 4% and 10%: (a) The contour shows the distribution of void volume fraction in the Al matrix, which accumulates in the thin ligaments between the alumina particles forming $\sim 45^\circ$ shear cracks as the strain reaches 10%; (b) The spatial distribution of matrix/particle decohesion damage variable (CSDMG) which illustrates more severely debonding failure compared to the Al-34 wt.% Al$_2$O$_3$ MMC (see Fig. 5(b)). This results in loss of stiffness and load sustaining capacity as shown in Fig. 4 (see the solid blue curve); (c) The data illustrates the evolution of particle cracking initiating from the sharp corners within the RVE as the axial strain increases from 4% to 10%.

6(b) and (c)) – which have been experimentally observed, as shown in Fig. 7 – and then propagate within the RVE. These failure mechanisms are accompanied by matrix failure due to void growth in the thin ligaments (see Fig. 6(a)). Once the strain exceeds 5%, the stress bearing capacity starts to decrease slightly and then remains constant up to a strain of 12% (Fig. 4 – the solid blue curve). This is a consequence of the development of the damage modes. The elements of the Al matrix in which the porosity has exceeded the critical value are removed from the mesh, leading to an abrupt decrease in load sustaining capacity (see Fig. 4 – the solid blue curve at the strain of ~12%). This behavior is in agreement with the experimental trend that the material's load-sustaining ability decreases after a given strain is reached. Overall, the reasonable agreement between the numerical and experimental findings in terms of stress-strain behaviors and failure mechanisms reveal the applicability of the model to conduct parametric studies that translate into tailoring particle and concentration size to control competition between failure mechanisms towards improving strength-density tradeoffs.
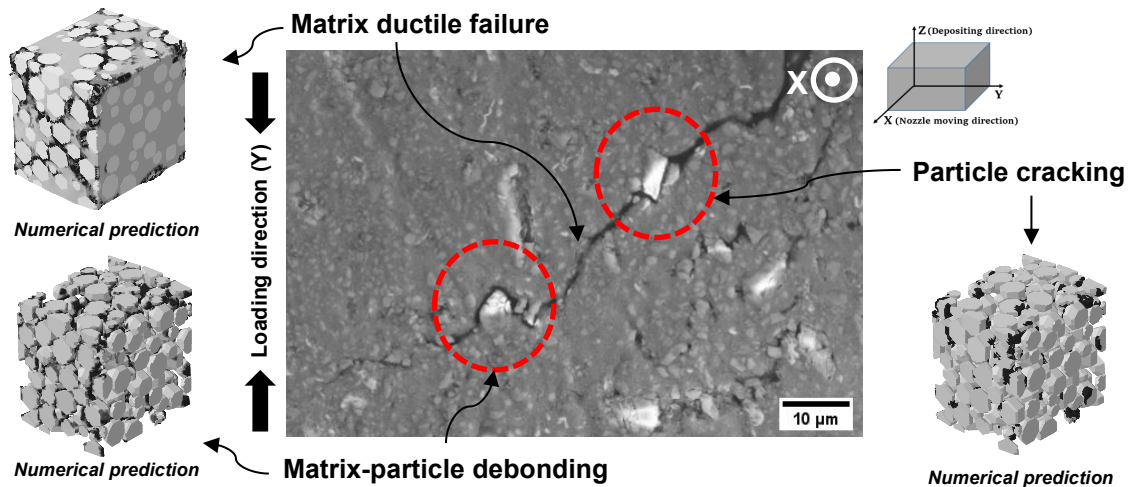

Fig. 7. SEM micrograph of the Al-46 wt.% Al$_2$O$_3$ MMC subject to quasi-static compression showing the simultaneous occurrence of failure mechanisms, namely matrix ductile failure, matrix/particle interfacial failure, and particle cracking. The 3D numerical predictions of the failure mechanisms (see Fig. 6 for more details) have been correspondingly shown, which confirm the qualitative validity of the model. The damaged areas are shown in black. Note that this micrograph represents the cuboidal sample loaded in Y direction and has been observed through X (i.e., the nozzle moving direction) direction.

4.2. *Vickers micro-indentation*

The numerical outcomes of the homogenization approach were validated by Vickers hardness experiments. In the experiments, Vickers micro-indentation was applied to the samples with a load of up to 10 N as per ASTM Standard E384 [70]. Figure 8(a) shows the plastically deformed area after complete unloading for the homogenized model of each MMC composite. From the figure, the diagonal length of the indented area decreased as the particle concentration increased, which results in a higher hardness. In other words, at a critical load, the composite material with a higher particle content is less deformed due to the enhanced stiffness and flow stress induced by the hard alumina particles.
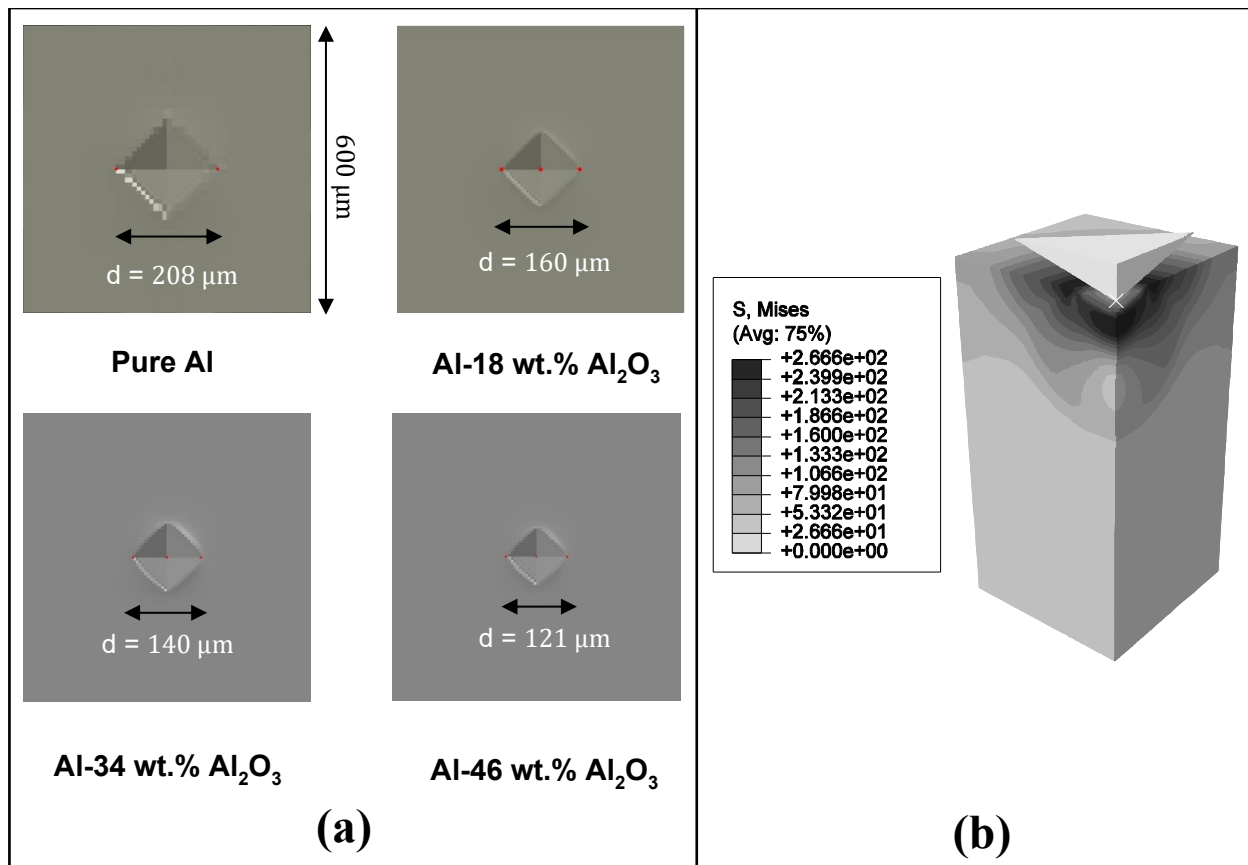

Fig. 8. (a) Numerical prediction of the indented area for the MMC composites based on the homogenization approach. The numerically measured diagonal length, *d*, of the indented profile is substituted into the Eq. (23) to calculate the Vickers hardness; (b) The distribution of the residual von Mises stress in the homogenized block of Al-34 wt.% Al_2O_3 composite after unloading.

Figure 8(b) illustrates the residual von Mises stress distribution for a load of 10 N after unloading in the homogenized model of Al-34 wt.% Al_2O_3 MMC. The distribution pattern for different particle concentrations is the same and the magnitude of the residual stress rises with an increase in the percentage of alumina particles. From Fig. 8(b), the residual stress follows a continuous distribution as the model does not explicitly account for the microstructure, while the observations reported after using 2D heterogeneous models [28,71] showed that the residual stress is localized between the particles. This implies that 3D microstructure-based models are needed to study how the residual stress is developed in the material more realistically. The Vickers hardness of the numerical data was computed using [72]:

$$HV \approx 0.1891 \frac{F}{d^2} \; [Kgf.mm^{-2}], \tag{25}$$

where F represents the applied load and d is the diagonal length of the indented area. Shown in Fig. 9 are the numerically predicted Vickers hardness results in comparison with the experimental ones measured in three different directions, namely the nozzle travel direction, the deposition direction, and the third perpendicular direction represented by X, Z, and Y, respectively, in the figure. As shown, the homogenized model predicts the hardness of MMCs with an error of $10 \pm 3\%$ compared to the measured values. The heterogeneous modeling approach was reported to overestimate the hardness of MMCs in previous studies [28,29,71,73] due to particle consolidation [74], which required calibration of a significant number of parameters to reach acceptable agreement with the experiments, when compared to the homogenization approach. However, a 3D microstructure-based model allows flexibility to investigate the effect of the size, randomness, and morphology of the particles on the indentation behavior and hardness of cold-sprayed MMC coatings.
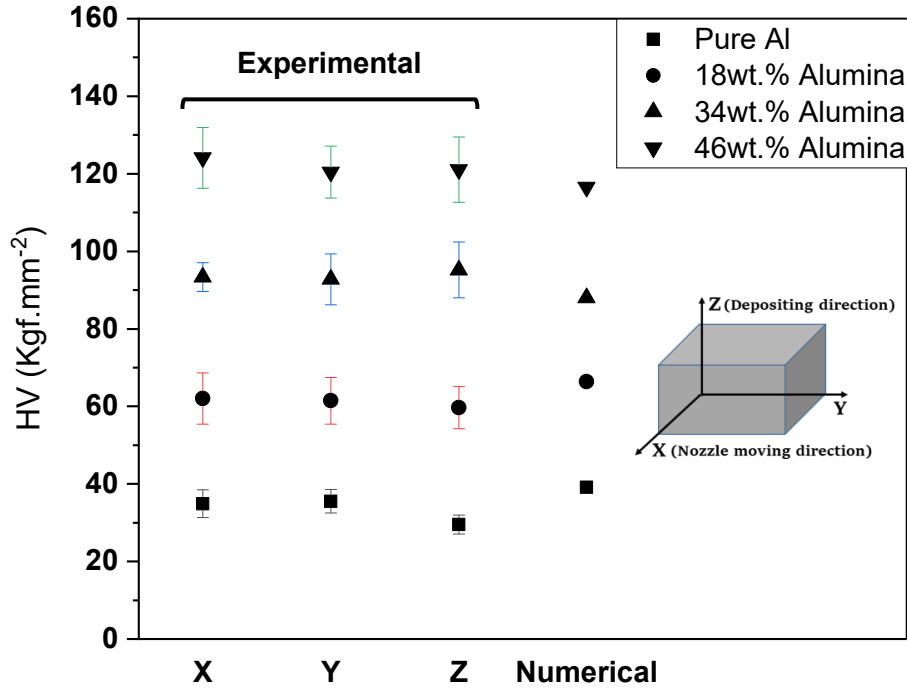
Fig. 9. Comparison of experimental and numerical Vickers hardness of the MMC coatings. The X, Y, Z on the horizontal axis represent the direction over which the Vickers indentation was carried out on the samples which correspond to the nozzle travel direction, the deposition direction, and the third perpendicular direction, respectively. Unlike the experimental results, there is no variation in the predicted hardness values due to the homogenization approach.

5. DISCUSSION

This study is the first of its kind to develop 3D finite element models to explore the compressive behavior and hardness of Al-Al₂O₃ composite coatings fabricated by low-pressure cold spray. The presented microstructure-based models for the MMC coatings were built on previous studies of 3D modelling of tensile behavior [10,11,13,37,75-78] and 2D modelling of the compressive response [54,68] of particulate-reinforced metal matrix composites. Our model culminated in an acceptable consistency between the numerical and experimental findings, both quantitatively (i.e., based on yield strain, yield strength, and stiffness) and qualitatively (i.e., based on initiation and propagation of damage mechanisms as well as the trends of stress versus strain histories), which lays the foundation to fill the gap in our computational knowledge of ceramic-metal composite

26

coatings. The extended 3D models of Al-Al$_2$O$_3$ MMC coatings were generated by Digimat software, where microstructural characteristics obtained by SEM micrographs and EDS analysis [33] were incorporated into the model, including the distribution of size, shape, and weight fraction (i.e., ~ 34wt. % and ~ 46wt. %) of reinforcing ceramic particles. Once the RVEs were generated, the models were validated using the experimental outcomes in terms of quantitative (i.e., stress versus strain histories) and qualitative (i.e., failure mechanisms) comparisons. This method of validation has also been used in previous studies [41,42,59,79]. The experimental measurements linked with the DIC technique showed that the compressive strength of the material was between 135 MPa and 178 MPa for the composite with 34wt. % of alumina and between 298 MPa and 317 MPa for the composite with 46wt. % of alumina. These are among the highest values reported in the literature [80-83] due to the fabrication strategy in this research that employs both matrix strengthening and dispersion strengthening mechanisms [33]. In addition, the measured stiffness of our coatings varied from 28 GPa to 62 GPa for the Al-34 wt. % Al$_2$O$_3$ composites and from 48 GPa to 63 GPa for the Al-46 wt.% Al$_2$O$_3$ composites. The developed model predicted the strength of the material with an error based on the average experimental quantities of 9.6% and 17.6% for the 34wt. % alumina and the 46wt. % alumina samples, respectively. As well, the numerical prediction of the stiffness yielded a value of 38 GPa and 53 GPa for the 34wt. % alumina and the 46wt. % alumina MMCs, respectively, resulting in an error of 15.5 % and 4.5% with respect to the average measured values. With the maximum error of 17.6%, the model is reasonably in quantitative agreement with the experimental outcomes. Qualitatively, for the first time to the best of our knowledge, the manifestation and evolution of experimentally observed failure mechanisms in ceramic-metal coatings under compression (i.e., matrix ductile failure, matrix/particle debonding, and particle cracking) were all numerically captured through a 3D micromechanical

finite element framework. This improves upon previous studies using 2D models [23,54,68] or single-particle 3D models [11]. Additionally, the necessity of developing 3D models in this study was illustrated by Böhm *et al.* [84] and Soppa *et al.* [85] to adequately capture the plastic strain distribution in two-phase materials.

Finally, the discrepancies between the simulation and experimental results can stem from the differences between the assumed and real boundary conditions [86], the complexities of the real microstructures such as clustering [79] that are not yet incorporated into the generated RVEs, the fracture of reinforcing particles during the cold spray deposition process [18] leading to damage accumulation, and the increase in porosity due to interface decohesion and particle cracking [87], which are not considered in the GTN model implemented in the present study. In addition, the work hardening effect [88] induced in the Al matrix by the high-velocity impact of hard ceramic particles gives rise to significant increase in dislocation density [89], which results in higher strength and hardness in the experimental samples when compared to the model predictions. To account for these crystallographic orientation effects [90] in the model, electron back scattering diffraction (EBSD)-based RVEs [91,92] can be employed in the future as a promising future direction to numerically explore the micromechanical behavior of MMC coatings. Altogether, the presented model established a reasonable match between the predicted and measured outcomes which allows for further exploration of the microstructure-property relationships of the material (i.e., the effect of matrix porosity [93] as well as particle size [2,94], shape [95], and distribution [96] of particles on the macro-scale behavior). This paves the way to create a 3D computational tool for the design and optimization of ceramic-metal cold-sprayed composite coatings via tailoring the microstructure.

6.   CONCLUSION

This study explored the behavior of Al-Al$_2$O$_3$ composite coatings under quasi-static compression and indentation loading via FE analysis, both quantitatively (i.e., stress versus strain response) and qualitatively (i.e., the manifestation of damage mechanisms, including matrix ductile failure, interfacial debonding, and particle cracking). For the FE models, 3D RVEs were generated by Digimat software based on the microstructural features of the MMC coating samples with different particle concentrations, and the homogenization approach was employed for modeling the Vickers micro-indentation test. To account for the matrix ductile failure and the matrix/particle decohesion, the GTN model and the CZM approach were employed, respectively. The ceramic particles were modeled using the phenomenological JH2 model to incorporate particle damage accumulation. The FE model was validated by stress-strain histories, Vickers hardness, and damage mechanisms obtained experimentally, and a reasonable agreement was observed between the results. Altogether, the outcomes of this study confirm the applicability of the model to be used as a computational tool for spatially tailoring matrix and particle properties and geometries to develop high-performing gradiented coating structures.

7.   ACKNOWLEDGEMENTS

8. REFERENCES

1. K.J. Hodder, H. Izadi, A.G. McDonald, A.P. Gerlich, Fabrication of aluminum–alumina metal matrix composites via cold gas dynamic spraying at low pressure followed by friction stir processing, *Mater. Sci. Eng. A*, 2012, 556, p 114-121

2. K.J. Hodder, J.A. Nychka, A.G. McDonald, Comparison of 10 μm and 20 nm Al-Al$_2$O$_3$ Metal Matrix Composite Coatings Fabricated by Low-Pressure Cold Gas Dynamic Spraying, *J. Therm. Spray Technol.*, 2014, 23(5), p 839-848

3. Y. Tao, T. Xiong, C. Sun, H. Jin, H. Du, T. Li, Effect of α-Al$_2$O$_3$ on the properties of cold sprayed Al/α-Al$_2$O$_3$ composite coatings on AZ91D magnesium alloy, *Appl. Surf. Sci.*, 2009, **256**(1), p 261-266

4. Q. Wang, Q. Sun, M.-X. Zhang, W.-J. Niu, C.-B. Tang, K.-S. Wang, X. Rui, L. Zhai, L. Wang, The influence of cold and detonation thermal spraying processes on the microstructure and properties of Al-based composite coatings on Mg alloy, *Surf. Coat. Technol.*, 2018, **352**, p 627-633

5. C. San Marchi, F. Cao, M. Kouzeli, A. Mortensen, Quasistatic and dynamic compression of aluminum-oxide particle reinforced pure aluminum, *Mater. Sci. Eng. A*, 2002, **337**(1), p 202-211

6. Yashpal, Sumankant, C.S. Jawalkar, A.S. Verma, N.M. Suri, Fabrication of Aluminium Metal Matrix Composites with Particulate Reinforcement: A Review, *Mater. Today: Proceedings*, 2017, **4**(2, Part A), p 2927-2936

7. J.M. Shockley, S. Descartes, P. Vo, E. Irissou, R.R. Chromik, The influence of Al2O3 particle morphology on the coating formation and dry sliding wear behavior of cold sprayed Al–Al$_2$O$_3$ composites, *Surf. Coat. Technol.*, 2015, **270**, p 324-333

8. O. Meydanoglu, B. Jodoin, E.S. Kayali, Microstructure, mechanical properties and corrosion performance of 7075 Al matrix ceramic particle reinforced composite coatings produced by the cold gas dynamic spraying process, *Surf. Coat. Technol.*, 2013, **235**, p 108-116

9. D. Giugliano, D. Barbera, H. Chen, N.-K. Cho, Y. Liu, Creep-fatigue and cyclically enhanced creep mechanisms in aluminium based metal matrix composites, *Eur. J. Mech. A Solids*, 2019, **74**, p 66-80

10. Q. Shen, Z. Yuan, H. Liu, X. Zhang, Q. Fu, Q. Wang, The damage mechanism of 17vol.%SiCp/Al composite under uniaxial tensile stress, *Mater. Sci. Eng. A*, 2020, **782**, p 139274

11. R. Balokhonov, V. Romanova, A. Kulkov, Microstructure-based analysis of deformation and fracture in metal-matrix composite materials, *Eng. Fail. Anal.*, 2020, **110**, p 104412

12. Y. Ma, Z. Chen, M. Wang, D. Chen, N. Ma, H. Wang, High cycle fatigue behavior of the in-situ TiB2/7050 composite, *Mater. Sci. Eng. A*, 2015, **640**, p 350-356

13. P. Peng, M. Gao, E. Guo, H. Kang, H. Xie, Z. Chen, T. Wang, Deformation behavior and damage in B4Cp/6061Al composites: An actual 3D microstructure-based modeling, *Mater. Sci. Eng. A*, 2020, **781**, p 139169

14. Z. Zhang, F. Liu, E.-H. Han, L. Xu, P.C. Uzoma, Effects of Al2O3 on the microstructures and corrosion behavior of low-pressure cold gas sprayed Al 2024-Al2O3 composite coatings on AA 2024-T3 substrate, *Surf. Coat. Technol.*, 2019, **370**, p 53-68

15. R. Fernandez, B. Jodoin, Cold Spray Aluminum–Alumina Cermet Coatings: Effect of Alumina Content, *J. Therm. Spray Technol.*, 2018, **27**(4), p 603-623

16. T. Peat, A. Galloway, A. Toumpis, P. McNutt, N. Iqbal, The erosion performance of particle reinforced metal matrix composite coatings produced by co-deposition cold gas dynamic spraying, *Appl. Surf. Sci.*, 2017, **396**, p 1623-1634

17. H. Assadi, H. Kreye, F. Gärtner, T. Klassen, Cold spraying – A materials perspective, *Acta Mater.*, 2016, **116**, p 382-407

18. L. He, M. Hassani, A Review of the Mechanical and Tribological Behavior of Cold Spray Metal Matrix Composites, *J. Therm. Spray Technol.*, 2020, **29**(7), p 1565-1608

19.   J.M. Shockley, E.F. Rauch, R.R. Chromik, S. Descartes, TEM microanalysis of interfacial structures after dry sliding of cold sprayed Al-Al$_2$O$_3$, *Wear*, 2017, **376-377**, p 1411-1417

20.   Y.T.R. Lee, H. Ashrafizadeh, G. Fisher, A. McDonald, Effect of type of reinforcing particles on the deposition efficiency and wear resistance of low-pressure cold-sprayed metal matrix composite coatings, *Surf. Coat. Technol.*, 2017, **324**, p 190-200

21.   L. Gyansah, N.H. Tariq, J.R. Tang, X. Qiu, B. Feng, J. Huang, H. Du, J.Q. Wang, T.Y. Xiong, Cold spraying SiC/Al metal matrix composites: effects of SiC contents and heat treatment on microstructure, thermophysical and flexural properties, *Mater. Res. Express*, 2018, **5**(2), p 026523

22.   G. Bolelli, A. Candeli, H. Koivuluoto, L. Lusvarghi, T. Manfredini, P. Vuoristo, Microstructure-based thermo-mechanical modelling of thermal spray coatings, *Mater. Des.*, 2015, **73**, p 20-34

23.   R.R. Balokhonov, V.A. Romanova, S. Schmauder, E.S. Emelianova, A numerical study of plastic strain localization and fracture across multiple spatial scales in materials with metal-matrix composite coatings, *Theor. Appl. Fract. Mech.*, 2019, **101**, p 342-355

24.   S.I. Gad, M.A. Attia, M.A. Hassan, A.G. El-Shafei, A random microstructure-based model to study the effect of the shape of reinforcement particles on the damage of elastoplastic particulate metal matrix composites, *Ceram. Int.*, 2020, doi.org/10.1016/j.ceramint.2020.09.189

25.   J. Zhang, Q. Ouyang, Q. Guo, Z. Li, G. Fan, Y. Su, L. Jiang, E.J. Lavernia, J.M. Schoenung, D. Zhang, 3D Microstructure-based finite element modeling of deformation and fracture of SiCp/Al composites, *Compos. Sci. Technol.*, 2016, **123**, p 1-9

26.   M.A. Eltaher, A. Wagih, Micromechanical modeling of damage in elasto-plastic nanocomposites using unit cell representative volume element and cohesive zone model, *Ceram. Int.*, 2020, doi.org/10.1016/j.ceramint.2020.01.046

27.   H.K. Park, J. Jung, H.S. Kim, Three-dimensional microstructure modeling of particulate composites using statistical synthetic structure and its thermo-mechanical finite element analysis, *Comput. Mater. Sci.*, 2017, **126**, p 265-271

28.   R. Ekici, M. Kemal Apalak, M. Yildirim, F. Nair, Simulated and actual micro-structure models on the indentation behaviors of particle reinforced metal matrix composites, *Mater. Sci. Eng. A* 2014, **606**, p 290-298

29.   A.S. Shedbale, I.V. Singh, B.K. Mishra, Heterogeneous and homogenized models for predicting the indentation response of particle reinforced metal matrix composites, *Int. J. Mech. Mater. Des.*, 2017, **13**(4), p 531-552

30.   V. Tvergaard, A. Needleman, Analysis of the cup-cone fracture in a round tensile bar, *Acta Metall.*, 1984, **32**(1), p 157-169

31.   G.I. Barenblatt, The Mathematical Theory of Equilibrium Cracks in Brittle Fracture, Advances in Applied Mechanicsed., H.L. Dryden, T. von Kármán, G. Kuerti, F.H. van den Dungen, L. Howarth, Eds., Elsevier, 1962, p 55-129

32.   G.R. Johnson, T.J. Holmquist, An improved computational constitutive model for brittle materials, *AIP. Conf. Proc.*, 1994, **309**(1), p 981-984

33.   C. Shao, C. Lo, K. Bhagavathula, A. McDonald, J. Hogan, High strength particulate aluminum matrix composite design: Synergistic strengthening strategy, *Compos. Commun.*, 2021, **25**, p 100697

34.   M.P. Dewar, A.G. McDonald, A.P. Gerlich, Interfacial heating during low-pressure cold-gas dynamic spraying of aluminum coatings, *J. Mater. Sci.*, 2012, **47**(1), p 184-198

35.   Vic-2D, Correlated Solutions Inc., Irmo, South Carolina. URL ⟨http:// correlatedsolutions.com/vic-2d/.

36.   "STM C1425-15, Standard Test Method for Monotonic Compressive Strength of Advanced Ceramics at Ambient Temperature", West Conshohocken (PA)

37.   S. Ma, X. Zhuang, X. Wang, 3D micromechanical simulation of the mechanical behavior of an in-situ Al3Ti/A356 composite, *Compos. Part. B-ENG.*, 2019, **176**, p 107115

38. M. Parsazadeh, G. Fisher, A. McDonald, J. Hogan, Computational investigation of the effect of microstructure on the scratch resistance of tungsten-carbide nickel composite coatings, *Wear*, 2021, **478-479**, p 203888

39. N.K. Sharma, R.K. Mishra, S. Sharma, 3D micromechanical analysis of thermo-mechanical behavior of Al2O3/Al metal matrix composites, *Comput. Mater. Sci.,* 2016, **115**, p 192-201

40. S. Sayahlatifi, G.H. Rahimi, A. Bokaei, The quasi-static behavior of hybrid corrugated composite/balsa core sandwich structures in four-point bending: Experimental study and numerical simulation, *Eng. Struct.*, 2020, **210**, p 110361

41. B. Amirian, H.Y. Li, J.D. Hogan, An experimental and numerical study of novel nano-grained ($\gamma+\alpha_2$)-TiAl/Al2O3 cermets, *Mater. Sci. Eng. A*, 2019, **744**, p 570-580

42. B. Amirian, H.Y. Li, J.D. Hogan, The mechanical response of a α_2(Ti3Al) + γ(TiAl)-submicron grained Al2O3 cermet under dynamic compression: Modeling and experiment, *Acta Mater.*, 2019, **181**, p 291-308

43. S. Gatea, H. Ou, B. Lu, G. McCartney, Modelling of ductile fracture in single point incremental forming using a modified GTN model, *Eng. Fract. Mech.*, 2017, **186**, p 59-79

44. A.L. Gurson, Continuum Theory of Ductile Rupture by Void Nucleation and Growth: Part I—Yield Criteria and Flow Rules for Porous Ductile Media, *J. Eng. Mater. Technol.*, 1977, **99**(1), p 2-15

45. G. Li, S. Cui, Meso-mechanics and damage evolution of AA5182-O aluminum alloy sheet Based on the GTN model, *Eng. Fract. Mech.*, 2020, **235**, p 107162

46. A. Kami, B.M. Dariani, A. Sadough Vanini, D.S. Comsa, D. Banabic, Numerical determination of the forming limit curves of anisotropic sheet metals using GTN damage model, *J. Mater. Process. Technol.*, 2015, **216**, p 472-483

47. F. Abbassi, S. Mistou, A. Zghal, Failure analysis based on microvoid growth for sheet metal during uniaxial and biaxial tensile tests, *Mater. Des.*, 2013, **49**, p 638-646

48. V. Tvergaard, Influence of void nucleation on ductile shear fracture at a free surface, *J. Mech. Phys. Solids*, 1982, **30**(6), p 399-425

49. C.C. Chu, A. Needleman, Void Nucleation Effects in Biaxially Stretched Sheets, *J. Eng. Mater. Technol.*, 1980, **102**(3), p 249-256

50. Abaqus, User's manual, Version 6.14, Dassault Systèmes, 2014.

51. N. Benseddiq, A. Imad, A ductile fracture analysis using a local damage model, *Int. J. Press. Vessel. Pip.*, 2008, **85**(4), p 219-227

52. J. Venkatesan, M.A. Iqbal, V. Madhu, Experimental and numerical study of the dynamic response of B4C ceramic under uniaxial compression, *Thin-Walled Struct.*, 2020, **154**, p 106785

53. M.R.I. Islam, J.Q. Zheng, R.C. Batra, Ballistic performance of ceramic and ceramic-metal composite plates with JH1, JH2 and JHB material models, *Int. J. Impact Eng*, 2020, **137**, p 103469

54. J.-T. Zhang, L.-S. Liu, P.-C. Zhai, Z.-Y. Fu, Q.-J. Zhang, The prediction of the dynamic responses of ceramic particle reinforced MMCs by using multi-particle computational micro-mechanical method, *Compos. Sci. Technol.*, 2007, **67**(13), p 2775-2785

55. Y. Zhu, G.R. Liu, Y. Wen, C. Xu, W. Niu, G. Wang, Back-Spalling process of an Al2O3 ceramic plate subjected to an impact of steel ball, *Int. J. Impact Eng*, 2018, **122**, p 451-471

56. D.S. Dugdale, Yielding of steel sheets containing slits, *J. Mech. Phys. Solids*, 1960, **8**(2), p 100-104

57. D.V. Kubair, P.H. Geubelle, Y.Y. Huang, Analysis of a rate-dependent cohesive model for dynamic crack propagation, *Eng. Fract. Mech.*, 2002, **70**(5), p 685-704

58. P. Camanho, C. Dávila, Mixed-Mode Decohesion Finite Elements for the Simulation of Delamination in Composite Materials, 2002

59. S.I. Gad, M.A. Attia, M.A. Hassan, A.G. El-Shafei, Predictive Computational Model for Damage Behavior of Metal-Matrix Composites Emphasizing the Effect of Particle Size and Volume Fraction, *Mater.*, 2021, **14**(9)

60. G.V. Jagadeesh, S. Gangi Setti, A review on micromechanical methods for evaluation of mechanical behavior of particulate reinforced metal matrix composites, *J. Mater. Sci.*, 2020, **55**(23), p 9848-9882

61. Q. Meng, Z. Wang, Prediction of interfacial strength and failure mechanisms in particle-reinforced metal-matrix composites based on a micromechanical model, *Eng. Fract. Mech.*, 2015, **142**, p 170-183

62. A. Sazgar, M.R. Movahhedy, M. Mahnama, S. Sohrabpour, Development of a molecular dynamic based cohesive zone model for prediction of an equivalent material behavior for Al/Al_2O_3 composite, *Mater. Sci. Eng. A*, 2017, **679**, p 116-122

63. X.-T. Luo, G.-J. Yang, C.-J. Li, Multiple strengthening mechanisms of cold-sprayed cBNp/NiCrAl composite coating, *Surf. Coat. Technol.*, 2011, **205**(20), p 4808-4813

64. J. Wang, C. Li, Y. Wan, C. Zhang, J. Ran, M.W. Fu, Size effect on the shear damage under low stress triaxiality in micro-scaled plastic deformation of metallic materials, *Mater. Des.*, 2020, **196**, p 109107

65. K.S. Tun, V. Tungala, Q.B. Nguyen, J. Chan, R. Kwok, J.V.M. Kuma, M. Gupta, Enhancing tensile and compressive strengths of magnesium using nanosize (Al2O3 + Cu) hybrid reinforcements, *J. Compos. Mater.*, 2011, **46**(15), p 1879-1887

66. C.S. Pande, K.P. Cooper, Nanomechanics of Hall–Petch relationship in nanocrystalline materials, *Prog. Mater Sci.*, 2009, **54**(6), p 689-706

67. H. Lim, C.C. Battaile, J.E. Bishop, J.W. Foulk, Investigating mesh sensitivity and polycrystalline RVEs in crystal plasticity finite element simulations, *Int. J. Plast.*, 2019, **121**, p 101-115

68. J.-T. Zhang, H.-J. Shi, L.-S. Liu, P.-C. Zhai, Numerical analysis on the effects of particle configuration on the damage and mechanical properties of particle reinforced MMCs under dynamic compression, *Comput. Mater. Sci.*, 2010, **50**(2), p 496-502

69. G. Munday, J. Hogan, A. McDonald, On the microstructure-dependency of mechanical properties and failure of low-pressure cold-sprayed tungsten carbide-nickel metal matrix composite coatings, *Surf. Coat. Technol.*, 2020, **396**, p 125947

70. "Standard Test Method for Knoop and Vickers Hardness of Materials", E 384, Annual Book of ASTM Standards, ASTM, 2010, p 1-42

71. R. Ekici, M. Kemal Apalak, M. Yıldırım, F. Nair, Effects of random particle dispersion and size on the indentation behavior of SiC particle reinforced metal matrix composites, *Mater. Des.*, 2010, **31**(6), p 2818-2833

72. ISO 6507-1: Metallic materials – Vickers hardness test – Part 1: Test method

73. Y.L. Shen, Y.L. Guo, Indentation modelling of heterogeneous materials, *Modell. Simul. Mater. Sci. Eng.*, 2001, **9**(5), p 391-398

74. R. Pereyra, Y.L. Shen, Characterization of Indentation-induced 'Particle Crowding' in Metal Matrix Composites, *Int. J. Damage Mech.*, 2005, **14**(3), p 197-213

75. J.F. Zhang, H. Andrä, X.X. Zhang, Q.Z. Wang, B.L. Xiao, Z.Y. Ma, An enhanced finite element model considering multi strengthening and damage mechanisms in particle reinforced metal matrix composites, *Compos. Struct.*, 2019, **226**, p 111281

76. L. Weng, T. Fan, M. Wen, Y. Shen, Three-dimensional multi-particle FE model and effects of interface damage, particle size and morphology on tensile behavior of particle reinforced composites, *Compos. Struct.*, 2019, **209**, p 590-605

77. X. Gao, X. Zhang, M. Qian, L. Geng, Effect of reinforcement shape on fracture behaviour of SiC/Al composites with network architecture, *Compos. Struct.*, 2019, **215**, p 411-420

78. J.F. Zhang, X.X. Zhang, Q.Z. Wang, B.L. Xiao, Z.Y. Ma, Simulations of deformation and damage processes of SiCp/Al composites during tension, *J. Mater. Sci. Technol*, 2018, **34**(4), p 627-634

79. S. Ma, X. Zhuang, X. Wang, Particle distribution-dependent micromechanical simulation on mechanical properties and damage behaviors of particle reinforced metal matrix composites, *J. Mater. Sci.*, 2021, **56**(11), p 6780-6798

80. S. Amirkhanlou, M.R. Rezaei, B. Niroumand, M.R. Toroghinejad, Refinement of microstructure and improvement of mechanical properties of Al/Al$_2$O$_3$ cast composite by accumulative roll bonding process, *Mater. Sci. Eng. A*, 2011, **528**(6), p 2548-2553

81. D. Garbiec, M. Jurczyk, N. Levintant-Zayonts, T. Mościcki, Properties of Al–Al2O3 composites synthesized by spark plasma sintering method, *Arch. Civ. Mech. Eng.*, 2015, **15**(4), p 933-939

82. M. Rahimian, N. Parvin, N. Ehsani, Investigation of particle size and amount of alumina on microstructure and mechanical properties of Al matrix composite made by powder metallurgy, *Mater. Sci. Eng. A*, 2010, **527**(4), p 1031-1038

83. M.P. Reddy, F. Ubaid, R.A. Shakoor, G. Parande, V. Manakari, A.M.A. Mohamed, M. Gupta, Effect of reinforcement concentration on the properties of hot extruded Al-Al$_2$O$_3$ composites synthesized through microwave sintering process, *Mater. Sci. Eng. A*, 2017, **696**, p 60-69

84. H.J. Böhm, W. Han, Comparisons between three-dimensional and two-dimensional multi-particle unit cell models for particle reinforced metal matrix composites, *Modell. Simul. Mater. Sci. Eng.*, 2001, **9**(2), p 47-65

85. E. Soppa, J. Nellesen, V. Romanova, G. Fischer, H.-A. Crostack, F. Beckmann, Impact of 3D-model thickness on FE-simulations of microstructure, *Mater. Sci. Eng. A*, 2010, **527**(3), p 802-811

86. H. Qing, Automatic generation of 2D micromechanical finite element model of silicon–carbide/aluminum metal matrix composites: Effects of the boundary conditions, *Mater. Des.*, 2013, **44**, p 446-453

87. K. Dorhmi, L. Morin, K. Derrien, Z. Hadjem-Hamouche, J.-P. Chevalier, A homogenization-based damage model for stiffness loss in ductile metal-matrix composites, *J. Mech. Phys. Solids*, 2020, **137**, p 103812

88. A. Góral, W. Żórawski, M. Makrenek, The effect of the standoff distance on the microstructure and mechanical properties of cold sprayed Cr3C2-25(Ni20Cr) coatings, *Surf. Coat. Technol.*, 2019, **361**, p 9-18

89. B. Liu, W. Huang, L. Huang, H. Wang, Size-dependent compression deformation behaviors of high particle content B4C/Al composites, *Mater. Sci. Eng. A*, 2012, **534**, p 530-535

90. M. Groeber, S. Ghosh, M.D. Uchic, D.M. Dimiduk, A framework for automated analysis and simulation of 3D polycrystalline microstructures.: Part 1: Statistical characterization, *Acta Mater.*, 2008, **56**(6), p 1257-1273

91. J. Genée, S. Berbenni, N. Gey, R.A. Lebensohn, F. Bonnet, Particle interspacing effects on the mechanical behavior of a Fe–TiB$_2$ metal matrix composite using FFT-based mesoscopic field dislocation mechanics, *Adv. Model. Simul. Eng. Sci.*, 2020, **7**(1), p 6

92. W. Kayser, A. Bezold, C. Broeckmann, EBSD-based FEM simulation of residual stresses in a WC6wt.-%Co hardmetal, *Int. J. Refract. Met. Hard Mater.*, 2018, **73**, p 139-145

93. W. Jibran, J. Hogan, A. McDonald, Towards optimization of thickness, hardness, and porosity of low-pressure cold sprayed WC-Ni coatings, *Int. J. Adv. Manuf. Tech.*, 2021, doi.org/10.1007/s00170-021-07500-w

94. J. Liu, X. Huang, K. Zhao, Z. Zhu, X. Zhu, L. An, Effect of reinforcement particle size on quasistatic and dynamic mechanical properties of Al-Al$_2$O$_3$ composites, *J. Alloys Compd.*, 2019, **797**, p 1367-1371

95. A. Rasool, H.J. Böhm, Effects of particle shape on the macroscopic and microscopic linear behaviors of particle reinforced composites, *Int. J. Eng. Sci.*, 2012, **58**, p 21-34

96. Q. Liu, F. Qi, Q. Wang, H. Ding, K. Chu, Y. Liu, C. Li, The influence of particles size and its distribution on the degree of stress concentration in particulate reinforced metal matrix composites, *Mater. Sci. Eng. A*, 2018, **731**, p 351-359

9.   LIST OF TABLES

Table 1: GTN model constants used in this study. Here, the value of f_0 corresponds to the composites with 34wt.% of reinforcing particles. For Al-46 wt.% Al_2O_3 composites, the initial porosity was determined to be 0.0023 on average.

Table 2: The JH2 constants used for Al_2O_3 reinforcing particles [54,55].

Table 3: Summary of the matrix/particle interface properties.

10.   LIST OF FIGURES

Fig. 1: Fig. 1. Preparation, test, and characterization of Al-Al_2O_3 composite coatings: (a) A schematic illustration of the cold spray setup used for the fabrication of pure Al and MMC coating samples: The processing strategy for making the mixed powder includes gas atomization, sieving, and mixing using a rotated cylinder; (b) Typical compressive cuboidal specimen with dimensions 2.3 mm × 2.7 mm × 3.5 mm cut from the composite depositions via wire electrical discharge machining, which was loaded in the direction of the 3.5 mm dimension. The green contour shows the region of interest defined on the specimen surface in VIC-2D software for monitoring the strain fields. The top image shows an example of Al-Al_2O_3 coating deposited on an Al substrate from which the cuboidal specimens were cut; (c) SEM characterization of the microstructure of Al-34 wt.% Al_2O_3 composite coating showing the distribution and morphology of the reinforcing ceramic particles in the Al matrix; (d) SEM micrograph of Al-46 wt.% Al_2O_3 composite coating. Note that

the black arrows on the SEM micrographs show the deposition direction. The darker regions correspond to the Al phase and the lighter regions correspond to the alumina phase.

Fig. 2: (a) Application of kinematic coupling between the boundary faces and the reference points (RP) in yellow color to apply compressive load and boundary conditions: All degrees of freedom were coupled to each other; (b) The boundary conditions applied on the RVE: The displacement control technique was applied to the RP in red color using a smooth amplitude to meet the quasi-static condition.

Fig. 3: Finite element model of the micro-indentation Vickers test. The block and the indenter were discretized by 30,276 first order 8-node 3D elements with reduced integration (C3D8R) and 2104 quadrilateral 4-node 3D rigid elements (R3D4), respectively.

Fig. 4: Numerical (Num) and experimental (Exp) stress-strain responses under quasi-static compression for different weight percentage of alumina in the Al matrix. The cuboidal samples were all tested in three different directions denoted by X, Y, and Z corresponding to the nozzle moving direction, the second in-plane direction perpendicular to the nozzle moving direction, and the deposition direction, respectively. The dashed curves correspond to the experimental responses for each coating and the solid curves represent the associated numerically predicted behavior.

Fig. 5. The numerically predicted manifestation and evolution of the damage mechanisms in Al-34 wt.% Al_2O_3 MMC at an axial strain of 4% and 10%: (a) The equivalent plastic strain (PEEQ), which reveals the evolution of plastic deformation in the thin ligaments between the ceramic

particles; (b) The data shows the scatter of matrix/particle debonding failure criterion demonstrating the initiation of interfacial failure at the sharp corners of inclusions; (c) The distribution of the JH2 damage parameter shows the accumulation of damage and element removal in the concaves of particles either at the boundary surfaces or considerably close to each other; (d) SEM micrograph of the Al-34 wt.% Al_2O_3 MMC subject to quasi-static compression showing the localized occurrence of damage mechanisms (e.g., matrix ductile failure, and matrix/particle decohesion) at micro length scale that does not lead to the coalescence of micro cracks and global failure of the composite at macro scale.

Fig. 6: The numerical qualitative results for the Al-46 wt.% Al_2O_3 MMC shown at an axial strain of 4% and 10%: (a) The contour shows the distribution of void volume fraction in the Al matrix, which accumulates in the thin ligaments between the alumina particles forming $\sim 45°$ shear cracks as the strain reaches 10%; (b) The spatial distribution of matrix/particle decohesion damage variable (CSDMG) which illustrates more severely debonding failure compared to the Al-34 wt.% Al_2O_3 MMC (see Fig. 5(b)). This results in loss of stiffness and load sustaining capacity as shown in Fig. 4 (see the solid blue curve); (c) The data illustrates the evolution of particle cracking initiating from the sharp corners within the RVE as the axial strain increases from 4% to 10%.

Fig. 7: SEM micrograph of the Al-46 wt.% Al_2O_3 MMC subject to quasi-static compression showing the simultaneous occurrence of failure mechanisms, namely matrix ductile failure, matrix/particle interfacial failure, and particle cracking. The 3D numerical predictions of the failure mechanisms (see Fig. 6 for more details) have been correspondingly shown, which confirm the qualitative validity of the model. The damaged areas are shown in black. Note that this

micrograph represents the cuboidal sample loaded in Y direction and has been observed through X (i.e., the nozzle moving direction) direction.

Fig. 8: (a) Numerical prediction of the indented area for the MMC composites based on the homogenization approach. The numerically measured diameter, *d*, of the indented profile is substituted into the Eq. (23) to calculate the Vickers hardness; (b) The distribution of the residual von Mises stress in the homogenized block of Al-34 wt.% Al_2O_3 composite after unloading.

Fig. 9: Comparison of experimental and numerical Vickers hardness of the MMC coatings. The X, Y, Z on the horizontal axis represent the direction over which the Vickers indentation was carried out on the samples which correspond to the nozzle travel direction, the deposition direction, and the third perpendicular direction, respectively. Unlike the experimental results, there is no variation in the predicted hardness values due to the homogenization approach.